Ambient seismic noise monitoring and imaging at the Theistareykir geothermal field (Iceland)

Toledo, Tania; Obermann, A.; Verdel, A.; Martins, Joana E.; Jousset, P.; Mortensen, A. K.; Erbas, Kemal; Krawczyk, C. M.

DOI
10.1016/j.jvolgeores.2022.107590

Publication date
2022

Document Version
Final published version

Published in
Journal of Volcanology and Geothermal Research

Citation (APA)
Toledo, T., Obermann, A., Verdel, A., Martins, J. E., Jousset, P., Mortensen, A. K., Erbas, K., & Krawczyk, C. M. (2022). Ambient seismic noise monitoring and imaging at the Theistareykir geothermal field (Iceland). *Journal of Volcanology and Geothermal Research*, *429*, Article 107590. https://doi.org/10.1016/j.jvolgeores.2022.107590

Journal of Volcanology and Geothermal Research 429 (2022) 107590

Contents lists available at ScienceDirect

Journal of Volcanology and Geothermal Research

journal homepage: www.journals.elsevier.com/journal-of-volcanology-and-geothermal-research

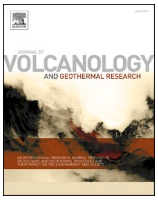

Ambient seismic noise monitoring and imaging at the Theistareykir geothermal field (Iceland)

T. Toledo[a,b,c,*], A. Obermann[c], A. Verdel[d], J.E. Martins[d,e], P. Jousset[a], A.K. Mortensen[f], K. Erbas[a], C.M. Krawczyk[a,b]

[a] GFZ German Research Centre for Geosciences, Potsdam, Germany
[b] TU Berlin, Berlin, Germany
[c] SED, ETH, Zurich, Zurich, Switzerland
[d] TNO, Utrecht, the Netherlands
[e] TU Delft, Delft, the Netherlands
[f] Landsvirkjun, Iceland

ARTICLE INFO

Keywords:
Geothermal exploration
Seismic imaging
Seismic monitoring
Ambient noise

ABSTRACT

In autumn 2017 a network of 14 broadband seismic stations was deployed at the Theistareykir high temperature geothermal field (NE Iceland). This experiment was conducted as part of the current efforts to characterize the field's main structures, and possible short and long term stress variations due to the ongoing fluid injection and extraction operations which started in autumn 2017. In this work, we use two years of continuous seismic records (October 2017–October 2019) to compute a 3D shear wave velocity model of the geothermal field and to detect possible crustal stress changes related to the injection and production activities. From phase cross-correlations of the vertical component recordings, we measure the Rayleigh wave group velocity dispersion curves to obtain 2D group velocity maps between 1 and 5 s. Subsequently, we use a neighborhood algorithm to retrieve the 3D shear wave velocity model of Theistareykir. Mainly, two sets of elongated high and low velocity anomalies can be observed oriented in a NW/WNW direction, parallel to the lineaments of the active Tjörnes fracture zone. Velocity reductions west of Ketilfjall and at Baerjafjall could indicate the location of upflow zones of the magmatic reservoir or hydrothermal system. We analyzed the temporal evolution of phase and amplitude of phase auto-correlations using the stretching technique and discuss their behavior in relation to the geothermal field operations. We notice a slightly stronger long-term velocity decrease in the reservoir region compared to outer regions. This could be related to the mass depletion in that area (higher fluid extraction compared to the water reinjection). In summary, our findings show how a monitoring network can be set up to enable a detailed imaging and monitoring of reservoir behavior in general.

1. Introduction

Theistareykir is a high temperature geothermal field located in NE Iceland (Fig. 1a). It is situated atop the Mid-Atlantic Ridge (MAR), at the divergent boundary between the North American and the Eurasian plates, a region rich in recent volcanism, seismicity, and geothermal activity. Theistareykir was first investigated in the 70s in association to native sulfur mining (Grönvold and Karlsdóttir, *1975*). Further research was conducted in the early 80s in Iceland's efforts to systematically identify potential sites for geothermal heat and electricity production (Ármannsson et al., 1986). Electric production at Theistareykir started, however, in late 2017 due to its larger distance to populated areas compared to other identified high temperature geothermal resources. Until 2021, 17 deep wells were drilled with depths ∼ 2.5 km. The recorded temperatures exceed 300°C at 1.1 km depth in most wells, with the hottest well registering temperatures exceeding 350°C at 2 km depth (Khodayar et al., 2018). Since spring 2018, the geothermal power plant at Theistareykir generates 90 MW electric power and is operated by the national power company of Iceland (Landsvirkjun) (Landsvirkjun, *2016*).

First gravity, aeromagnetic, geologic, and tectonic maps were reported by Grönvold and Karlsdóttir *(1975)* and Gíslason et al. *(1984)*.

---

* Corresponding author at: GFZ German Research Centre for Geosciences, Potsdam, Germany.
E-mail address: tania.toledo@sed.ethz.ch (T. Toledo).

https://doi.org/10.1016/j.jvolgeores.2022.107590
Received 6 August 2021; Received in revised form 20 May 2022; Accepted 21 May 2022

Between 1981 and 1984, Layugan (1981); Gíslason et al. *(1984)*; Ármannsson et al. (1986); Darling and Ármannsson (1989) made first major geothermal assessments indicating an *E*-W enlongated heat source extending across a N-S tectonic structure (fissure swarm) connected to the active Theistareykir central volcano. From 1991 to 2000, the Theistareykir area was monitored intermittently (Ármannsson et al., *2000*). Later, Gautason et al. *(2000)* gathered the available knowledge to recommend first drilling sites which started in 2002.

First Transient Electro Magnetism (TEM) soundings were performed by Karlsdóttir et al. *(2006)*. Later, Karlsdóttir et al. *(2012)* computed a 3D inversion of Magneto-Telluric (MT) and TEM data to obtain the field's resistivity structure and better estimate the geometry of the heat source, the extents of the low resistivity cap, and the locations of upflow zones of geothermal fluid into the system. An uplift was reported below the Theistareykir area using GPS and InSAR techniques which was likely caused by magma accumulation at ~8.5 km depth between 2007 and 2008 (Spaans et al., 2012; Metzger et al., 2011). Khodayar and Björnsson *(2013)* used aerial photos to identify the region's fracture patterns. Khodayar et al. *(2015, 2018)* combined the available geophysical results with geological mapping, surface alteration, gas geochemistry, and water geochemistry (Gíslason et al., *1984*; Saemundsson, 2007; Kristinsson et al., 2013a, 2013b; Óskarsson, 2011) in a multidisciplinary analysis that defined the basis for the continuation of drilling targets at Theistareykir. Finally, Blanck et al. (2017a, 2017b, 2018, 2020) recorded and analyzed the local seismicity at Theistareykir using a seismic network of five stations, and the efforts to monitor the local seismicity are still ongoing.

The start of electric production in 2017 triggered new studies to improve the characterization and monitoring of Theistareykir prior and during production. In this framework, a multiparameter network was installed to monitor the geothermal field's response to the start and ongoing operations. A set of 27 time-lapse micro-gravity stations were measured at different time periods in 2017, 2018, and 2019 to analyze the field's mass distribution changes (Portier et al., 2020). These data were complemented with 4 permanent gravity stations, 3 of which equipped with superconducting gravity meters deployed at the injection and extraction areas (Erbas et al., 2020; Forster et al., 2021). These permanent stations are equipped with GPS receivers, tiltmeters, and meteorological stations. Vertical displacements of periods prior and during production were obtained through an InSAR analysis by Drouin (2020). Finally, a set of 14 seismic broadband stations was deployed to support the permanent monitoring and to provide detailed insights on the seismicity, underground structure, and stress and deformation changes of the geothermal field (Erbas et al., 2020; Naranjo, 2020; Ágústsson et al., 2020). The present study expands on the available knowledge of the geothermal field and newly acquired seismic data to investigate the seismic structure and temporal velocity changes at Theistareykir.

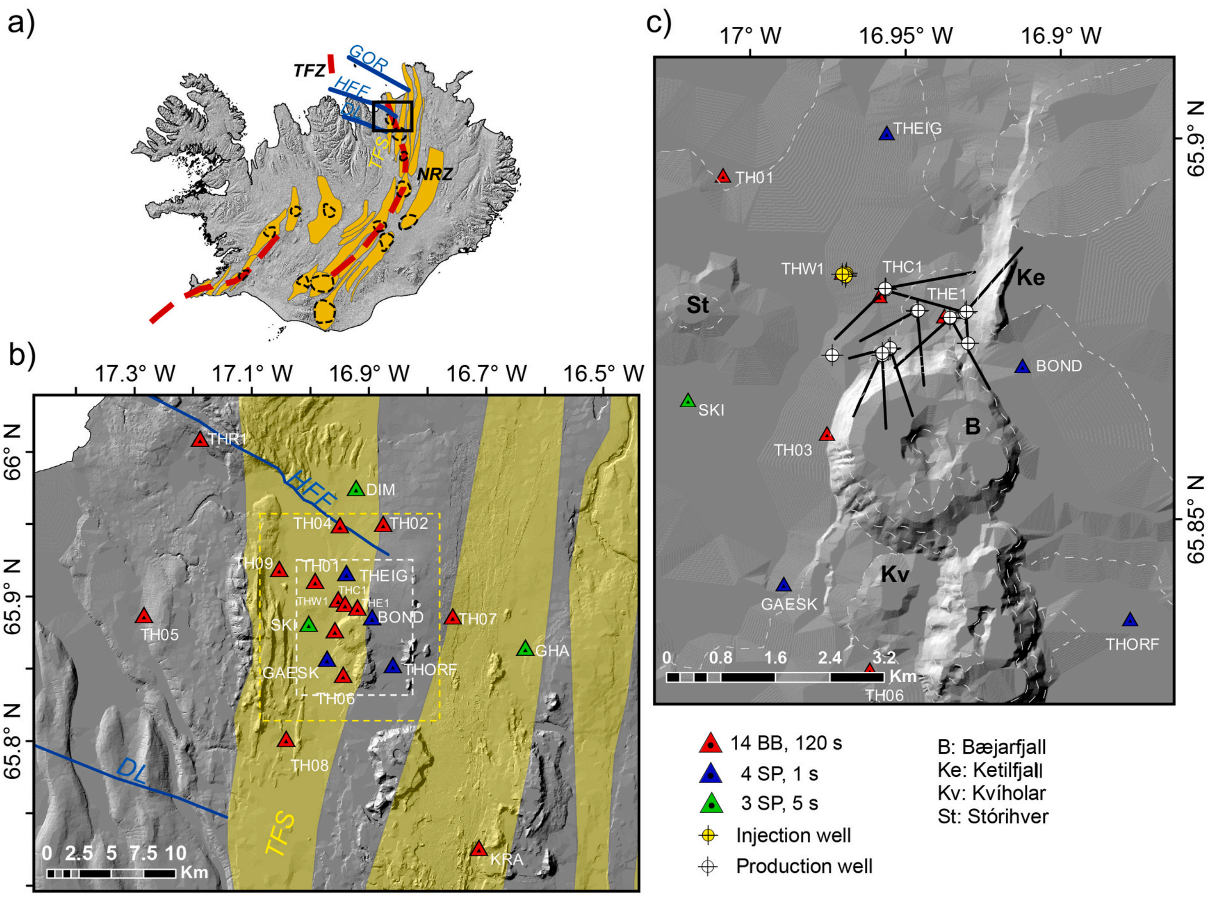

Fig. 1. a) A simplified tectonic map of Iceland showing the location of the Theistareykir geothermal field (black square) (modified from Árnason, 2020). Red broken lines show the spreading zones of the MAR, thin black broken lines show central volcanoes, and yellow areas indicate fissure swarms. The lineaments GOR (Grímsey Oblique-Rift), HFF (Húsavík-Flatey Fault), and DL (Dalvík Lineament) of the TFZ (Tjörnes Fracture Zone) are shown with blue lines. The TFS (Theistareykir fissure swarm) of the NRZ (Northern Rift Zone) is indicated with yellow letters. b) Temporary (red triangles) and permanent (blue and green triangles) seismic networks at the Theistareykir geothermal field. The location of panel c) is shown with white dashed lines. The yellow dashed lines indicate the region shown in Fig. 6. The HFF and DL are shown with blue lines, and the fissures swarms are indicated as yellow areas. c) Main exploitation area. The location of injection and production wells are marked with yellow and white circles, respectively. Approximate well deviations are shown as black lines. (For interpretation of the references to colour in this figure legend, the reader is referred to the web version of this article.)

Local earthquake tomography (LET) is a technique commonly used to investigate deep structures in seismically active geothermal settings (e.g. De Matteis et al., 2008; Karastathis et al., 2011; Jousset et al., 2011; Muksin et al., 2013; Calò and Dorbath, 2013; Toledo et al., 2020). 3D compressional P- (Vp) and shear S- (Vs) wave velocity models are obtained using P- and S-wave arrival times from local earthquakes (Thurber, 1983; Kissling, 1988). Although LET provides reliable information of the subsurface, high resolution is limited to regions characterized by high seismicity rates and adequate ray coverage (homogeneous distribution of local earthquakes and seismic stations), which is not given at Theistareykir, where the seismicity is mostly clustered at the producing geothermal field (Blanck et al., *2018, 2020*; Naranjo, 2020). Only a recent regional LET at the Tjörnes Fracture Zone was computed, however, with limited resolution at the Theistareykir area (Abril et al., 2021).

Ambient noise tomography (ANT) is an alternative method that is receiving increasing attention in geothermal exploration due to its increased resolution at shallow depth (e.g. Lehujeur et al., 2017; Martins et al., 2020b,2020a; Granados et al., 2020; Planès et al., 2020; Sánchez-Pastor et al., 2021). ANT is based on the reconstruction of Green's functions between different receiver pairs retrieved from the cross-correlation of long duration ambient noise records (Wapenaar, 2004; Shapiro et al., 2005; Wapenaar and Fokkema, 2006).

Noise-based methods have also been applied for the monitoring of geothermal/volcanic systems. Small elastic and structural changes in the medium are detected by measuring the temporal fluctuations (changes) of the multiple scattered waves called *coda* waves (Snieder, 2002; Sens-Schönfelder and Wegler, 2006; Obermann and Hillers, 2019). This technique is often referred to as coda wave interferometry (CWI). Obermann et al. (2015) used CWI to detect gas infiltration in the St. Gallen geothermal site (Switzerland). Similarly, Hillers et al. (2015) detected structural changes due to a reservoir stimulation in Basel (Switzerland). Taira et al. (2018) measured the response of the Salton Sea geothermal field (California) to earthquakes and fluid extraction; all three applications in sedimentary settings. Sánchez-Pastor et al. (2019) applied CWI to a volcanic setting, reporting on short and long-term variations of the Reykjanes geothermal field (Iceland); due to injection and production activities. Cubuk-Sabuncu et al. (2021) monitored the temporal velocity changes during the 2020 rapid inflation at Mt.Þorbjörn-Svartsengi (Iceland) and correlated these changes with InSAR and GPS deformation measurements.

In this study, we image the 3D Vs structure and assess the temporal velocity variations at the Theistareykir geothermal field using seismic interferometry. In section 2, we report on the geological setting and the seismic network deployed at Theistareykir. We describe the data processing steps to retrieve the surface Rayleigh waves in section 3. Section 4 addresses the 3D ambient seismic noise Rayleigh wave tomography. We assess the time-lapse velocity changes using CWI in section 5. Finally, section 6 discusses the obtained results in relation to existing and newly acquired geophysical and geological data.

2. Geologic setting and seismic network

2.1. Geologic and tectonic setting

The MAR spreads at an average rate of 2 cm/year (Einarsson, 2008). In Iceland, the MAR consists of a series of active rift and transform segments that bring forth numerous high temperature areas with the potential for geothermal energy exploitation. Theistareykir is located at the intersection between the active Northern Rift Zone (NRZ) and the active Tjörnes Fracture Zone (TFZ) (Fig. 1a).

The TFZ consists of three main WNW lineaments: the Grímsey Oblique Rift (GOR), the Húsavík-Flatey Fault (HFF), and the Dalvík Lineament (DL). It is characterized by dextral and dip slip-motions, and high seismicity rates (Stefánsson et al., 2008). The NRZ comprises five en echelon spreading segments, each with a fissure swarm and an associated central volcano responsible for the volcanic and high-temperature geothermal activities (Saemundsson, 1979; Einarsson and Sæmundsson, 1987; Pedersen et al., 2009). The Theistareykir Fissure Swarm (TFS) is the westernmost of them (Fig. 1b), with a roughly 9 km wide area and N-S extensional fractures that extend towards the sea (Thoroddsen, 1983; Magnúsdóttir and Brandsdóttir, 2011; Saemundsson et al., *2012*; Khodayar et al., 2018; Tibaldi et al., 2019, 2020). More specifically, our study area lies mainly between the TFS, and the HFF and DL lineaments (Fig. 1b).

At the surface, Theistareykir is mostly covered by lava flows that erupted during the late stages of the last glacial termination and early Holocene (Saemundsson, 2007) forming large volume volcanic shields. At the eastern edge of the geothermal field, Ketilfjall is the oldest hyaloclastite formation (Ke in Fig. 1c) and was formed during the eruption of a 4 km long fissure below the Quaternary ice-sheet. Further south, two younger table mountains (Baejarfjall -B- and Kvíhólafjöll -Kv- in Fig. 1c) were formed by eruptions on short fissures or single volcanic events (Gautason et al., 2010). The surface geothermal activity is most intense to the north and northwestern slopes of Baejarfjall and from there northwards to the western part of Ketilfjall (Ármannsson et al., *2000*).

Stratigraphically, the top ∼ 1 km is characterized by pillow basalts, breccias, and tuff (Gautason et al., 2010; Thorsteinsdóttir et al., *2018*), with the uppermost ∼ 400–800 m consisting in a zeolite/smectite zone (low resistivity cap, Karlsdóttir et al., *2012*). Below ∼ 800 m.b.s.l. sits a sequence of basaltic lavas, with lenses of breccias and glassy basalt (Gautason et al., 2010). This sequence is cut by fresh vertical or sub-vertical intrusions or basaltic dykes (Gautason et al., 2010) and is also reflected as a high resistivity core (chlorite/epidote zone, Karlsdóttir et al., *2012*). The boundary between the cap rock and the resistive core comprises the 230–240°C temperature boundary (Karlsdóttir et al., *2012*). Finally, at ∼ 1.5 km b.s.l. lies the dolerite/gabbro bedrock (Thorsteinsdóttir et al., *2018*). Deep low resistivity bodies suggest that upflow zones of geothermal fluids are located below Ketilfjall (∼ 2 km b.s.l.), Bæjarfjall (∼ 6 km b.s.l.), and north of Stórihver (∼ 8 km b.s.l.) (Karlsdóttir et al., *2012*). Karlsdóttir et al. *(2012)* suggest that the prominent low resistivity anomaly at Ketilfjall could correspond to the main heat source of the geothermal system.

2.2. Seismic network

In September 2017, a temporary seismic network comprising 14 three-component broadband (Trillium Compact 120 s) sensors was deployed to record continuous seismic data at a sampling rate of 200 Hz (red triangles in Fig. 1b and Fig. 1c) (Erbas et al., 2021). This network was originally designed to monitor the local microseismicity associated with the exploitation of the geothermal field (Toledo et al., 2018). Two permanent seismic networks within the region add 4 short period 3DLite MkII (1 s) sensors (blue triangles in Fig. 1b and Fig. 1c) and 3 short period LE-3D 5 s sensors (green triangles in Fig. 1b and Fig. 1c). These networks are operated by the Icelandic Geosurvey (ISOR) and Landsvirkjun, and the Icelandic Meteorological Office (IMO), respectively.

3. Data processing

In this study we analyze the continuous seismic records between September 2017 and October 2019. We cut the seismic traces of the vertical components into 2 h long segments. Then, we downsample the traces to 5 Hz, apply a band-pass filter between 0.1 and 2.0 Hz, and remove the instrumental response using the MSNoise Python package (Lecocq et al., 2014).

We compute the cross correlations and auto correlations using a phase cross correlation approach (PCC; Schimmel, 1999; Ventosa et al., 2019). The PCC functional is based on the coherence of instantaneous phases of analytical traces. Its main advantage over the classical cross-correlation scheme (Bensen et al., 2007) is that it is amplitude unbiased and therefore does not require any preprocessing that could reduce waveform coherence (Schimmel et al., 2011, 2018). This technique has successfully been used in other noise-based studies for imaging and monitoring (e.g. D'Hour et al., 2015; Sánchez-Pastor et al., 2018, 2019; Acevedo et al., 2019; Hable et al., 2019; Crowder et al., 2020; Andreé et al., 2020).

Finally, we obtain daily correlation functions by stacking them linearly over a 5 and 10 day sliding data window for monitoring structural changes in the media, and over their full recording period to compute the ambient noise tomography. In the latter case, we additionally average positive and negative lag-times to enhance the symmetric part of the signal and to increase the signal-to-noise ratio (SNR) (e.g. Obermann et al., *2016*).

4. Ambient noise tomography

4.1. Group velocity dispersion analysis

We perform a Frequency Time Analysis (FTAN, Levshin et al., 1989) to extract the group velocity dispersion curves from the retrieved PCCs. Then, we manually revise and pick the fundamental mode of the dispersion curves for inter-station distances larger than 1.5 wavelengths and SNR $\geq$ 10 (e.g. Mordret et al., 2015; Obermann et al., *2016*; Planès et al., 2020). Fig. A.9a in the supplementary material shows the complete set of extracted group velocity dispersion curves. An increment in group velocities is seen from ~ 1.6–2.3 km/s to ~ 1.8–2.6 km/s with increasing periods for most dispersion curves. The dispersion curves are, however, quite dispersed and not clustered around one velocity value. Based on the number of measurements per period (Fig. A.9b in the supplementary material), we restrict our analysis to the range between 1 and 5 s, where we have at least 50 measurements and have better confidence in the picks.

We display the raypath maps at two different periods to assess the quality of our dataset in terms of regional coverage, cross-firing, and velocity outliers (Fig. 2a and Fig. 2c). Note the increase in velocities with increasing period, especially to the west and to the south east of the geothermal field.

We discretize the study area into cells of ~ 3.5 × 3.5 km. This value was chosen after testing taking into account the raypath distribution and the resulting spatial resolution. We chose the smallest cell size that would maintain, as much as possible, a homogeneous ray density (and few data gaps) especially around the center of the geothermal field. Fig. 2b and Fig. 2d shows the ray path density (number of rays per cell) associated with the chosen grid discretization for 2 and 5 s. Notice the inhomogeneous ray density distribution for both periods due to the

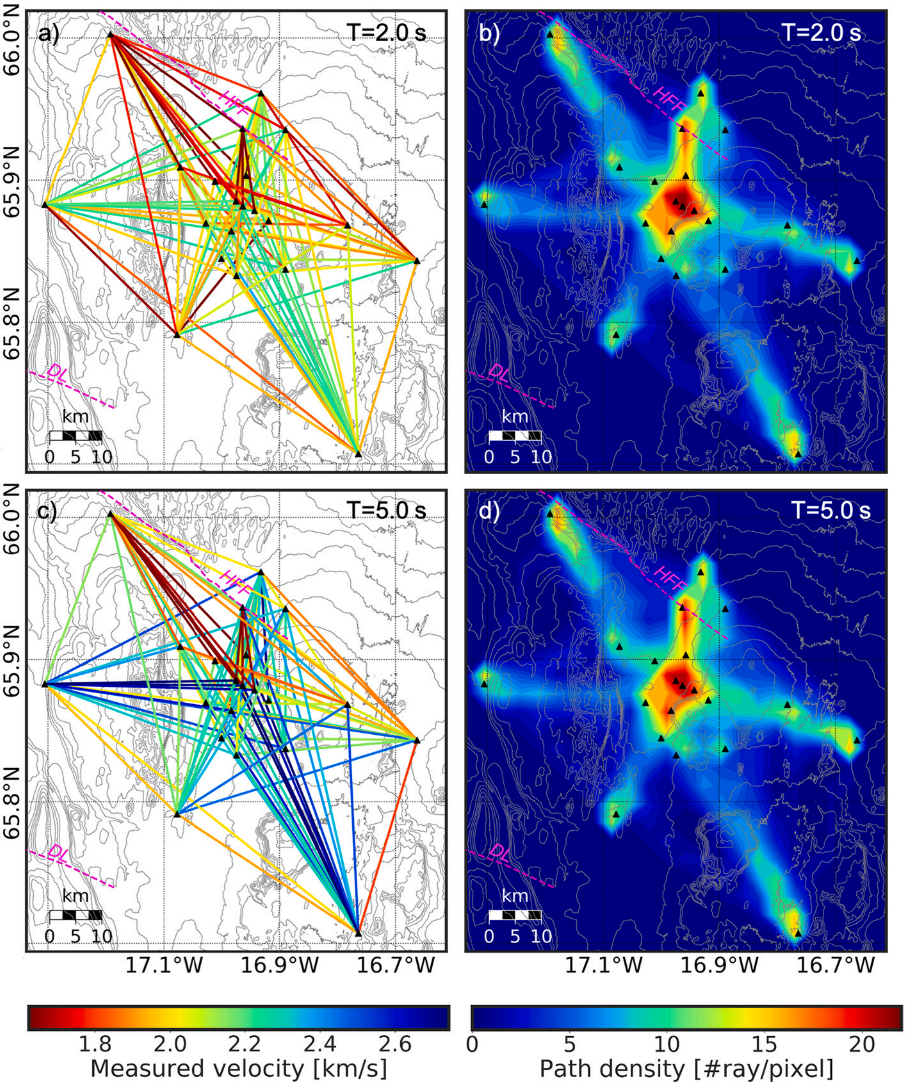

Fig. 2. Raypath (a, c) and ray density (b, d) maps for periods of 2 and 5 s. Raypaths in a) and c) are colored with their associated measured group velocity. The chosen cell size is ~ 3.5 × 3.5 km. Black trianges indicate the seismic stations positions and the gray lines correspond to topographic contours. DL and HFF correspond to the Dalvík Lineament and the Húsavik-Flatey Fault, respectively.

irregular seismic network configuration, originally deployed for recovering local seismicity. A higher ray density is observed towards the center of the geothermal field, where a higher number of closely spaced stations are located.

4.2. 2D group velocity tomography

We perform 40 tomographic inversions for periods between 1 and 5 s with 0.1 s steps following the methodology proposed by Barmin et al. (2001) and Mordret et al. (2013). The inversions are based on ray theory coupled with a damping constraint and a Gaussian-shaped lateral smoothing term. Group times for each period are calculated by integrating the group slowness along each ray path. We ignore the topography effects, assuming they are negligible on the retrieved traveltimes (elevation difference of 301 m vs a wavelength of ~ 2 km at 1 s).

The 2D inversions are performed in 2 steps. A first inversion is computed for each period using the mean group velocity as the initial model. The aim is to reject measurements with time residuals larger than 0.01 standard deviations (e.g. Mordret et al., 2015). The remaining travel times are then used in a second and final inversion using the obtained velocities of the previous step as the initial model. We select the values of 0.01, 0.01, 1.0, and 0.01 for parameters alpha, beta, lambda, and Lcorr (Barmin et al., 2001; Mordret et al., 2013), respectively, for the two inversion steps. These parameters were chosen after computing inversions for a range of values and comparing their associated variance reduction of traveltime residuals.

Fig. 3a-d illustrate the obtained group velocities at periods of 2, 3, 4, and 5 s, respectively. Following the inversions, the residuals variance is reduced by ~80 % for all periods. The group velocities increase with greater periods and range between 1.62 and 2.74 km/s. Two sets of high and low velocity anomalies stretch with a NW-SE direction. High velocity anomalies are located to the west and to the southeast of the Baejarfjall table mountain. Low velocities appear to the north of Baejarfjall crossing the Ketilfjall ridge.

4.3. Model quality

To identify the location of poorly resolved areas we analyze the model resolution matrices (MRM) associated with the inversions. The diagonal elements of the MRM provide an estimate of the inversion resolution, namely how well the model parameters can be predicted or resolved. Off-diagonal elements contain information on the dependency

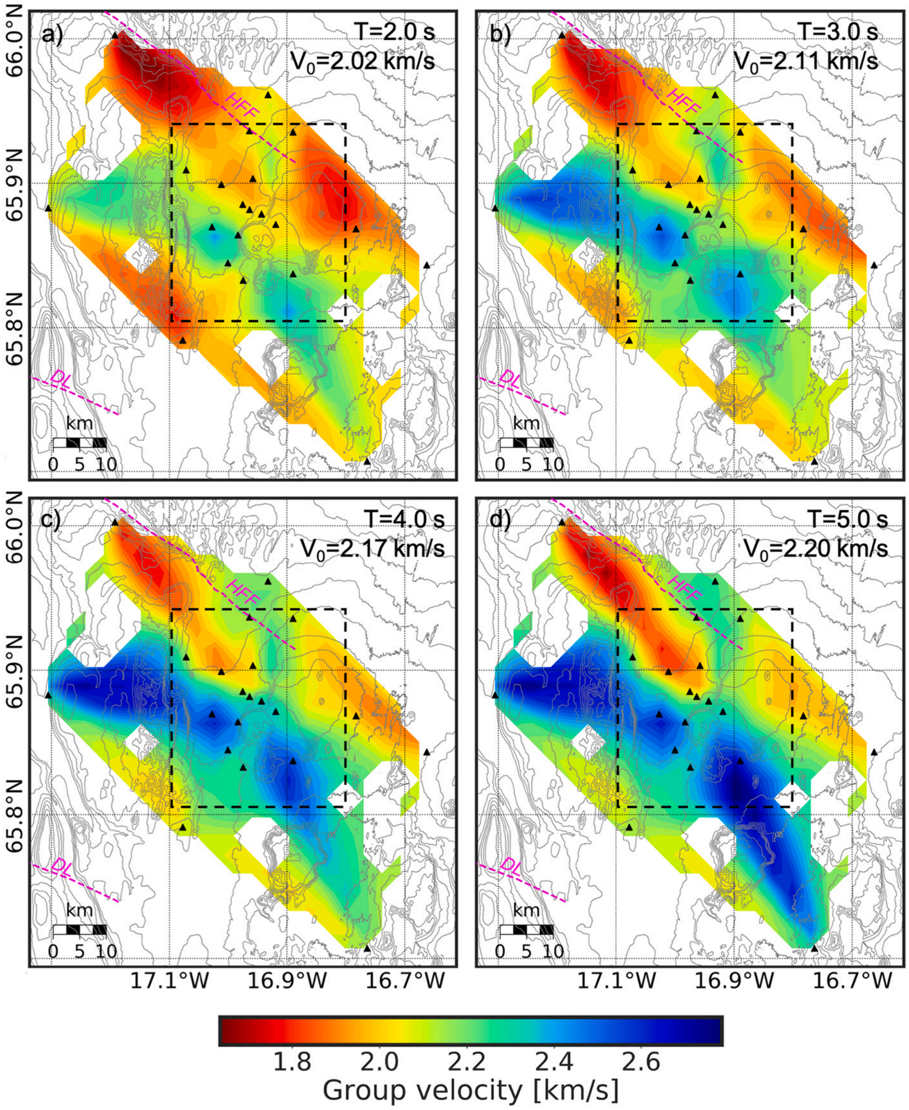

Fig. 3. Rayleigh wave group velocity maps at a) 2, b) 3, c) 4, and d) 5 s. Initial velocities used in each inversion are shown in the upper right corner. Black trianges indicate the seismic stations positions and the gray lines correspond to topographic contours. DL and HFF correspond to the Dalvík Lineament and the Húsavik-Flatey Fault, respectively. The black dashed lines indicate the region shown in Fig. 6.

of the solution of each cell with respect to neighboring cells.

As in Mordret et al. (2015), we define the spatial resolution as the equivalent diameter of a fitted ellipse to the contour level at 40 % of each row of the MRM. The minimal spatial resolution (or spatial detail) value is estimated as twice the distance between two cells, in this case ~ 7 km. Then the resolution shift (or spatial accuracy) is defined as the distance between the center of each fitted ellipse and the target cell. Fig. 4a and Fig. 4c show the calculated spatial resolution at 2 s and 5 s, respectively. The values range between 7 and ≥ 13 km, and are lower towards the main exploitation area, where the seismic array is denser. This central area is, therefore, expected to be better resolved in comparison to the surrounding regions. Similarly, Fig. 4b and Fig. 4d show the resolution shift for 2 and 5 s, respectively. Shift values are once more lower towards the center of the geothermal field. We display the contour level at 80 % (red lines in Fig. 4a-d) for three rows of the MRM to observe the direction of the smearing associated to three cells (red crosses in Fig. 4a-d). Seemingly, the contours at the center indicate a more focused solution, whereas the contours to the west indicate strong EW smearing due to a single ray direction (Fig. 2a and Fig. 2c). For the interpretation, we thus restrict our analysis to the center of the geothermal field (the region surrounding Baejarfjall).

4.4. Retrieval of the 3D Vs model

We perform a second series of inversions to associate the 2D Rayleigh group velocity results to a precise depth. First, we construct local group velocity dispersion curves at all cell points by combining the tomographic inversions with different periods. Each of these dispersion curves are then inverted to obtain single 1D local layered velocity models which are later assembled into the final 3D S-wave velocity (Vs) model.

The 1D velocity profiles are obtained following a Monte Carlo inversion approach called the Neighborhood Algorithm (NA, Sambridge, 1999). For each cell, we first generate a large set (N_{ini}) of random continuous Vs functions that are later discretized into layered models of constant thicknesses and velocities. We define these functions as power law velocity profiles overlaid by three splines to reduce the number of parameters to invert for (otherwise $2n_l$, where n_l is the number of layers) (Mordret et al., 2014, 2015). The associated dispersion curves are then calculated using the Computer Programs in Seismology package (Herrmann, 2013). We evaluate the misfit between these synthetic models and the data dispersion curves. Later, we select the N_b best fitting models and randomly resample N_r new models in their neighborhood. This procedure is carried out for N_{iter} iterations or until the misfit is reduced to a given threshold. In this work, we select $N_{ini} = 1000$, $N_b = 750$, $N_r = 2$, and $N_{iter} = 20$, giving a total of 31,000 probed models. Fig. A.10a and

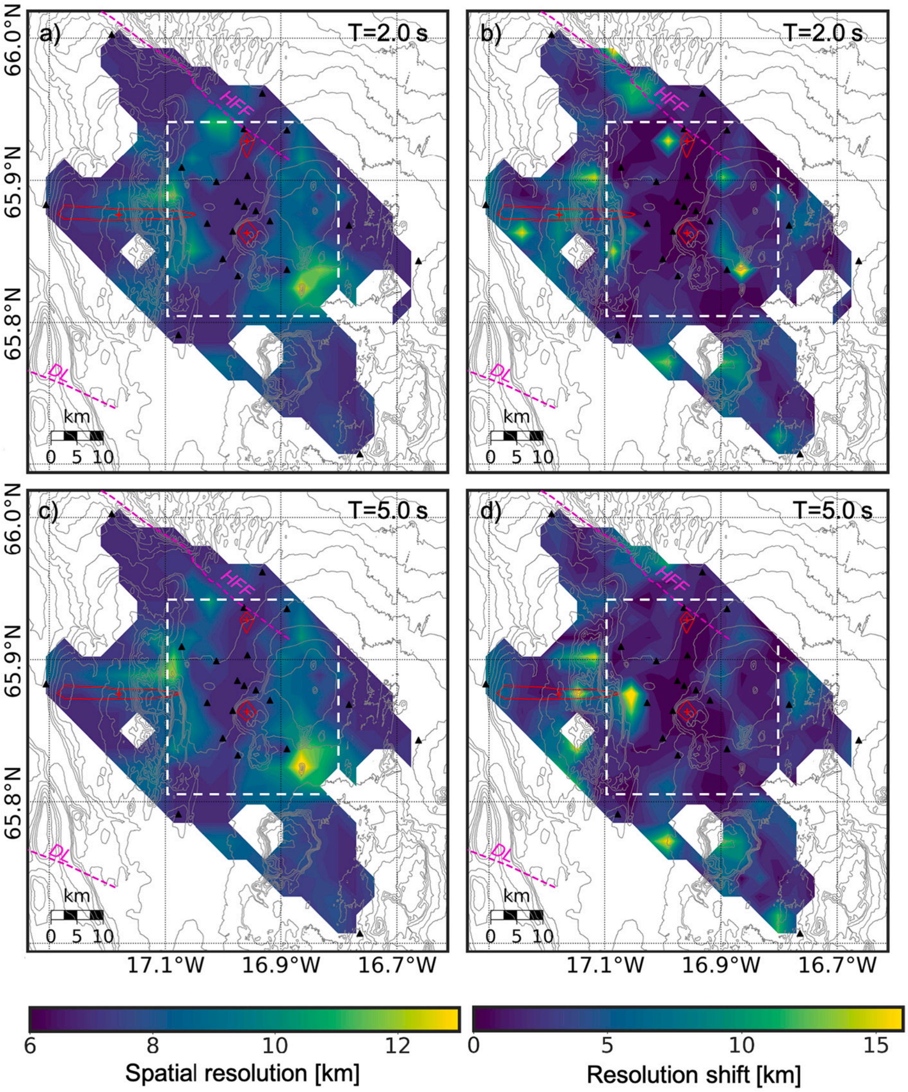

Fig. 4. Spatial resolution (a, c) and resolution shift (b, d) at 2 and 5 s. The red lines indicate the 80 % contour levels of the MRM associated to three cells points (red crosses). Black trianges indicate the seismic stations positions and the gray lines correspond to topographic contours. DL and HFF correspond to the Dalvík Lineament and the Húsavik-Flatey Fault, respectively. The white dashed lines indicate the region shown in Fig. 6. (For interpretation of the references to colour in this figure legend, the reader is referred to the web version of this article.)

Fig. A.10b in the supplementary material display an example of the synthetic dispersion curves and the associated 1D Vs models, respectively, for the 1D inversion of a single grid point. The lines in these figures are colored according to the logarithm of their misfit. Fig. 5 shows the recovered 1D Vs models for all the locations in the 2D plane. Up to $\sim$ 2 km depth, the models show a good agreement with the 1D Vs model used in Iceland for earthquake locations (South Iceland Lowland -SIL-model, Stefánsson et al., 1993; Abril et al., *2021*). After 2 km, however, the inverted values are lower than the SIL model. With the ambient noise methods used we obtain a higher resolution in the very shallow subsurface and a much more local model than the SIL model, which was calculated using the recovered seismicity over Iceland.

In Fig. 6a-f we present several depth slices of the retrieved 3D Vs model for the central part of the geothermal field. The model is presented as Vs variations (ΔVs) with respect to the mean value for each layer (V_0). Similar to the 2D group velocity maps, two main trends of anomalies are oriented in NW-SE direction extending to $<$ 4–5 km depth. Two high velocity anomalies ($\sim +10$ %) are located to the west and to the south of the Baejarfjall mountain, and become weaker at shallow and deeper levels ($\sim +6$ %). An elongated low velocity anomaly is located to the northeast of Baejarfjall, and is slightly discontinuous at the Ketilfjall formation. The low velocity anomaly to the west of Ketilfjall becomes stronger with depth ($\sim$ -9 % at $\geq$ 2 km b.s.l). North to this anomaly, another high velocity anomaly with smaller amplitude ($\sim +4$ %) is visible mostly at shallow levels ($\leq$ 2 km b.s.l).

5. Determination of time-lapse changes

Seismic monitoring using CWI has been successfully implemented in various applications (Obermann and Hillers, 2019) using techniques like the moving-window cross-spectra analysis (MWCS, Ratdomopurbo and Poupinet, 1995), the observation of waveform similarity evolution (D'Hour et al., 2015), and the stretching technique (Lobkis and Weaver, 2003; Sens-Schönfelder and Wegler, 2006). A thorough comparison between the MWCS and the stretching method was performed by Hadziioannou et al. (2009) showing more stable results for the latter. In this work, we compute and analyze the velocity variations using the stretching technique on the phase auto correlations (PAC) between October 2017 and October 2019. Auto correlations are known to be more sensitive to local changes than cross correlations and to probe larger depths (D'Hour et al., 2015; Sánchez-Pastor et al., 2018).

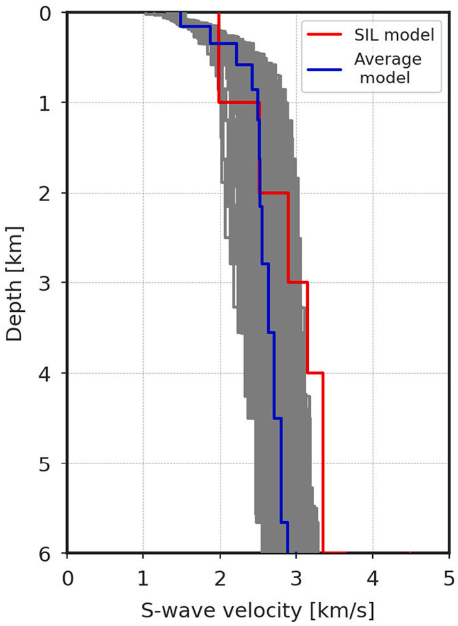

Fig. 5. Best fitting 1D Vs profiles for each grid cell (gray lines). The 1D model that is routinely used for earthquake locations in Iceland (SIL model, Stefánsson et al., 1993) is shown with a red line. (For interpretation of the references to colour in this figure legend, the reader is referred to the web version of this article.)

To quantify the temporal evolution of seismic velocities, we analyze the waveform changes of a "current" PAC^{curr} with respect to a reference PAC^{ref}. We define the PAC^{ref} as the stacked daily PACs over the entire recording period, and PAC^{curr} as the daily stacked PACs over a 5 and 10 day sliding window. Each PAC^{curr} is then stretched or compressed in time by a factor $t(1+\varepsilon)$ and compared to PAC^{ref}. The stretching factor ε by which the dilation correlation coefficient (CC) between PAC^{ref} and PAC^{curr} is maximized corresponds to the apparent velocity change ($\varepsilon^{app} = -\frac{\Delta v}{v}$)(Sens-Schönfelder and Wegler, 2006; Nakata et al., 2019).

The dilation correlation coefficient is given by (Weaver et al., 2011):

$$CC(\varepsilon) = \frac{\int_{t_1}^{t_2} PAC_{\varepsilon}^{curr}(t) PAC^{ref}(t) dt}{\sqrt{\int_{t_1}^{t_2} \left(PAC_{\varepsilon}^{curr}(t)\right)^2 dt \int_{t_1}^{t_2} \left(PAC^{ref}(t)\right)^2 dt}} \tag{1}$$

where PAC_{ε}^{curr} corresponds to the stretched PAC^{curr} function and t_1 and t_2 are the limits of the time window used. The uncertainty on $\frac{\Delta v}{v}$ is estimated with the theoretical formula (Weaver et al., 2011):

$$\sigma_{\varepsilon} = \frac{\sqrt{1-CC^2}}{2CC} \sqrt{\frac{6\sqrt{\frac{\pi}{2}}T}{\omega_c^2 (t_2^3 - t_1^3)}} \tag{2}$$

where T is the inverse of the frequency band and ω_c is the central frequency.

Fig. A.11 in the supplementary material displays the velocity variations computed on two PACs between 1 and 21 s lag time. The PACs are associated to a station close (TH03) and a station further away (TH05) from the geothermal site. Except for a few points, most CCs are $\sim$0.9, and the peak-to-peak velocity variations are $\sim$0.3 %. The most prominent feature in both cases is a sinusoid with period of $\sim$365 days, maxima in January 2018 and January 2019, and minima in August 2018 and August 2019. This sinusoid could be attributed to seasonal changes in the system. Additionally, similar short-term fluctuations at various lag times are visible in both curves which could be associated to a range of factors like weather and seismicity. Although both curves have similar shapes, the velocity changes for the station close to the geothermal area (TH03) has occasionally lower values than for the distant station (TH05).

We separate the stretching results of stations neighboring the geothermal field (red triangles in Fig. 7) and compare them to the results of distant stations (THR1, GHA, TH05, and KRA in Fig. 1a) to evaluate whether local changes can be observed due to the exploitation activities. The background map in Fig. 7 represents the near-Up velocity differences between periods 2015–2017 and 2017–2020 obtained with InSAR (taken from Drouin, 2020). Drouin (2020) estimate the approximate east (near-East) and approximate vertical (near-Up) velocities by combining the estimated average line-of-sight velocity fields of ascending and descending tracks of radar SAR observations. Given the assumptions considered in the decomposition process, Drouin and Sigmundsson (2019) and Drouin (2020) call the results "near-East" and "near-Up" instead of "East" and "Up" ground velocities.

We display the $\frac{\Delta v}{v}$ average of the two station groups in Fig. 8a-b. The results are very stable for the PACs. Both the sinusoidal behavior and several short term fluctuations are similar in both curves. However, it is noticeable that the $\frac{\Delta v}{v}$ for the station group located within/close to the geothermal field (red line) are, on average, lower than for those of the distant station group (blue line). When fitting the average velocity changes of these station groups to a linear function (Fig. 8c), we observe a slight larger velocity decrease for the curves associated to the geothermal field (-0.054 +/− 0.007 %/year vs -0.046 +/− 0.007%/year for outer stations). It must be pointed out, however, that linear regression operations could be underestimating the measurements

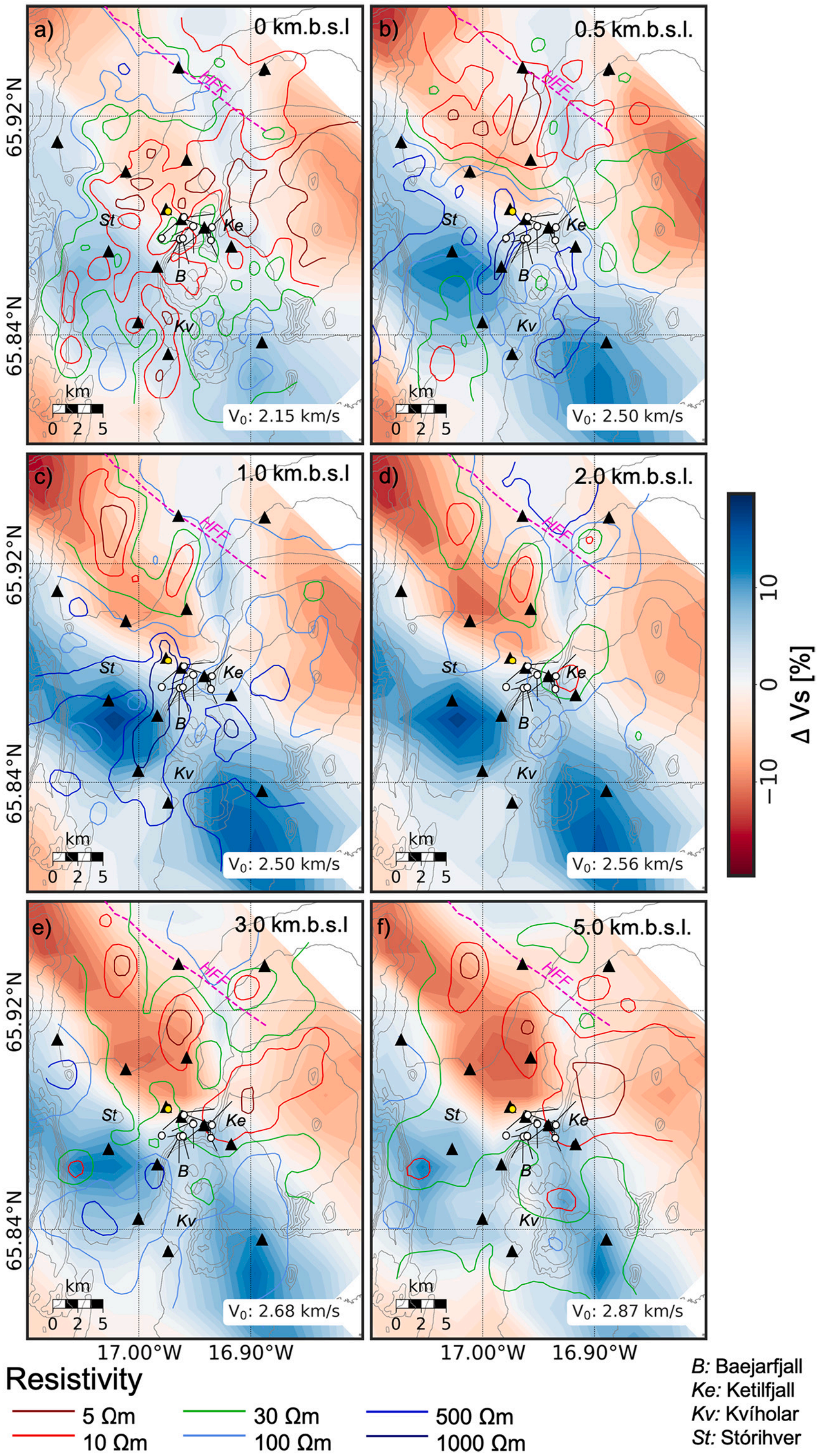

Fig. 6. Vs variation (ΔVs) depth slices with respect to the layer average (V_0). Resistivity contour lines are taken from Karlsdóttir et al. *(2012)*. Black triangles indicate the seismic stations positions and the gray lines correspond to topographic contours. White circles represent the location of injection and production wells, and the approximate well deviations are shown with black lines. The location of these maps is shown with yellow dashed lines in Fig. 1b. HFF indicates the Húsavik-Flatey Fault. (For interpretation of the references to colour in this figure legend, the reader is referred to the web version of this article.)

errors.

6. Interpretation and discussion

6.1. Ambient noise tomography

The ambient noise tomography in Section 4 (Fig. 6) shows a clear separation between low (N and NE of Baejarfjall) and high (W, S, and SW of Baejarfjall) velocity anomalies trending with a NW/WNW orientation. This direction is almost parallel to the HFF lineament (Fig. 1a), and follows the location of a series of fractures (narrow weak zones) with WNW and NW dextral oblique-slip mapped at the surface (Khodayar et al., 2018). The boundary of the velocity anomaly separation is located to the north of the Baejarfjall mountain, where the injection and several production wells are located. This pattern is consistent at all depth levels, and matches the direction of several MT resistivity anomalies plotted on top of the tomography results (colored line contours in Fig. 6, taken from Karlsdóttir et al., *2012*). A similar good match between resistivity and ambient noise tomography results has also been observed in Hengill (Sánchez-Pastor et al., 2021), thus highlighting the high

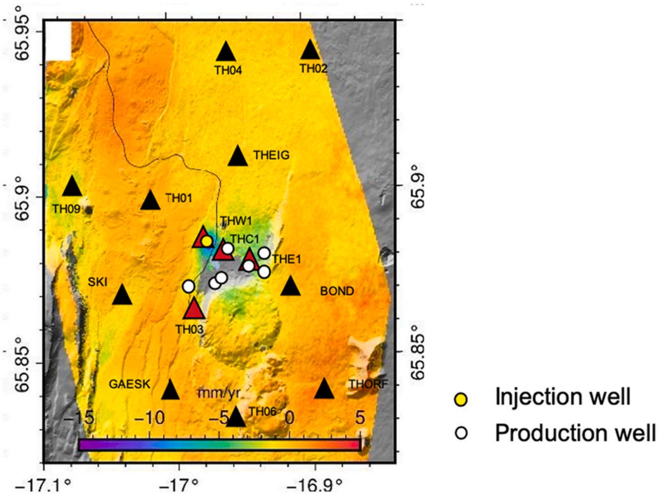

Fig. 7. The red triangles represent the selected stations for the time lapse analysis. The background map represents the near-Up velocity [mm/year] differences between periods 2015–2017 and 2017–2020 (Drouin, 2020) obtained with Synthetic Aperture Radar Interferometry (InSAR). The gray regions represent areas of missing data. (For interpretation of the references to colour in this figure legend, the reader is referred to the web version of this article.)

potential of ambient noise tomographic methods for geothermal exploration purposes.

The low velocity anomalies (~-7 %) to the N and NE coincide with the location of various low resistive bodies (Karlsdóttir et al., *2012*). One major low velocity anomaly to the north of Baejarfjall and west of Ketilfjall becomes stronger (~-10 %) starting from ~2 km b.s.l. (Fig. 6d-f). Studies have shown that rocks saturated with hydrothermal fluids have typically lower shear wave velocities than those of unaltered rocks (Vanorio et al., 2005; De Matteis et al., 2008). In a lithologically homogenous subsurface, the decrease of Vs in this region could point to the location of either magmatic material or an upflow zone. Such a hypothesis is consistent with the MT survey, which highlights the heat source(s) beneath Ketilfjall, Bæjarfjall, and north of Stórihver below a shallow cap rock composed of zeolite/ smectite alterations (Karlsdóttir et al., *2012*). This region to the north of Baejarfjall and west of Ketilfjall is also known to experience a decrease in microgravity variations (Portier et al., 2020; Forster et al., 2021) and negative vertical displacements (Drouin, 2020) with time. In addition, surface geothermal manifestations (Kristinsson et al., *2015*) and emanating gases (Gíslason et al., *1984*) have been reported mostly at the northern and northwestern flank of Bæjarfjall.

The high velocity anomalies (~+10 %) to the west and south/ southeast of Bæjarfjall coincide with medium to high resistivity bodies (≥ 100 Ωm) at depths between 0.5 and 3 km b.s.l. Between these two anomalies, a lower high velocity anomaly (~+5 %) sits below Bæjarfjall, which reduces its amplitude mostly at depths ≥3 km b.s.l. (~+1 %). This reduction could, once more, hint to the presence of hot fluids at Bæjarfjall. Another weaker high velocity anomaly is located further to

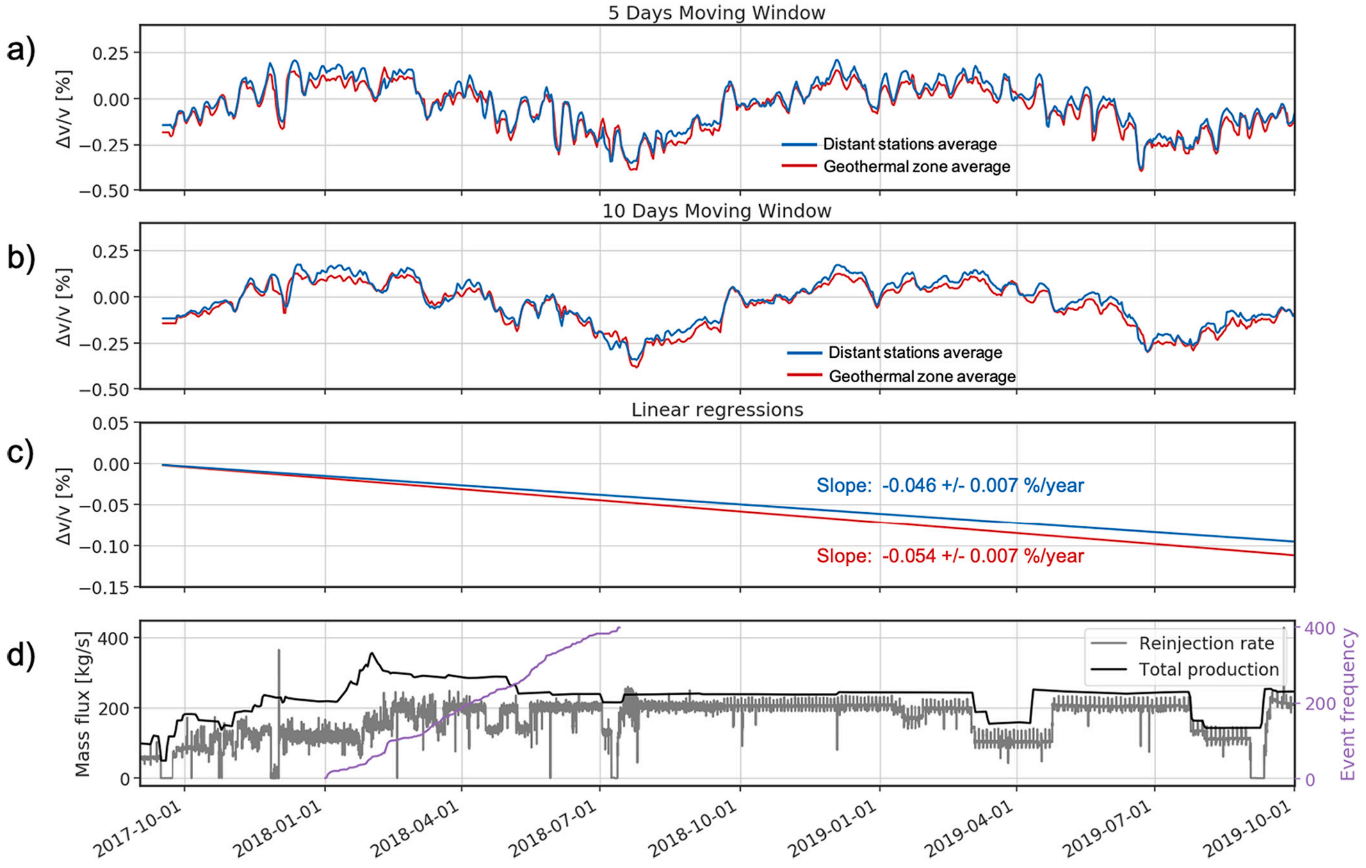

Fig. 8. Average velocity changes for two station groups: stations close to the geothermal zone (red stations in Fig. 7), and distant stations (THR1, GHA, TH05, and KRA in Fig. 1a). Results for a) 5 and b) 10 day stacks times. We discarded $\frac{\Delta v}{v}$ values with CC ≤ 0.7. c) Linear regressions of the velocity variation averages for the two station groups. d) Total extraction (black) and injection (gray) rates at the geothermal field, and local seismicity rates (purple) from 1 January 2018 to 15 July 2018 taken from (taken from Naranjo, 2020). See main text for more details. (For interpretation of the references to colour in this figure legend, the reader is referred to the web version of this article.)

the north following, once more, some resistive bodies.

6.2. Time-lapse changes

To analyze possible medium changes we monitor the differences between the PACs at different times with respect to a reference. In a geothermal context, some of these velocity variations have been successfully linked to the operation activities (e.g. Obermann et al., 2015; Hillers et al., 2015; Sánchez-Pastor et al., 2019). Fig. 8a-b show the velocity variations associated to the PACs of two station groups computed with the stretching technique. The red lines represent the velocity variations average for stations at/close to the geothermal field (Fig. 7) and the blue lines correspond to the velocity variations average of distant stations (THR1, GHA, TH05, and KRA in Fig. 1a). Several short term fluctuations are consistent among all the curves, however, most of them are difficult to directly associate to natural or man-made processes. The injection and extraction changes seem low for their effect to be seen in the $\frac{\Delta v}{v}$ short term fluctuations of the analyzed frequency band which has its highest sensitivity for the upper 5 km (see Fig. A.12 in the supplementary materials). Such observations are relevant for the sustainable continuation of geothermal operations at Theistareykir, however, an extended analysis using different frequency bands would be required for a more detailed analysis of different depths.

Long term noise studies typically exhibit seasonal variations (e.g. Sens-Schönfelder and Wegler, 2006; Sánchez-Pastor et al., 2019) which are evident in the distortion of ballistic waves (e.g. Hadziioannou et al., 2011). These variations could be the consequence of changes in the oceans noise sources at different seasons (Stutzmann et al., 2009), but could also be linked to the strong seasonal variations in Iceland that result in ground water level changes as seen in other case studies (e.g. Sens-Schönfelder and Wegler, 2006; Meier et al., 2010; Rivet et al., 2015; Almagro Vidal et al., 2021; Barajas et al., 2021). In this study, the seasonal variation appears as a sinusoidal trend which is evident for the $\frac{\Delta v}{v}$ curves of all station positions (Fig. 8a-b). We average the velocity variation curves for the two station groups and compute their linear regression to distinguish the difference between their long term variations (Fig. 8d). There is a small velocity decrease for both station groups. However this reduction is slightly stronger for the production area (0.054%/year vs 0.046%/year). Such a local decrease in velocities is consistent with the negative microgravity variations reported around the extraction zone (Portier et al., 2020; Forster et al., 2021). Additionally, (Drouin, 2020) reports a subsidence in this region of ~ 7 mm/year since the start of the operations in 2017 (Fig. 7).

7. Conclusions

Upon the deployment of a temporary seismic network at the Theistareykir geothermal field, we collected and analyze the ambient noise records of 2 years. We compute a 3D ambient noise Rayleigh wave tomography and compare the results with available geophysical, geochemical, and geological data. We could identify velocity anomalies oriented in a NW/WNW direction almost following the orientation of the HFF lineament. In addition, we identify a velocity reduction in two areas: one to the west of Ketilfjall (depths ≥ 2 km b.s.l.) and one at Baejarfjall (depths ≥ 3 km b.s.l.). We interpret these regions as locations of possible magmatic or hydrothermal bodies.

We compute the temporal velocity changes for the 2 year period using the stretching technique applied to PACs and compare the results associated to the stations close and far from the geothermal field. Several short term fluctuations are consistent among the $\frac{\Delta v}{v}$ curves, yet it is difficult to associate these fluctuations to man-made processes such as injection and extraction variations. Alternatively, the injection and extraction changes may be too low for their effect to be seen in the $\frac{\Delta v}{v}$ short term fluctuations. We, however, report a slightly higher long term velocity decrease (0.054%/year) within the geothermal system, which may be associated to the fluid extraction in this region.

In general, ambient noise methods hold a high potential for geothermal exploration and monitoring. The complementarity of ambient noise tomography with other geophysical, geological, and geochemical techniques enables a better understanding of geothermal resources. In addition, the monitoring of seismic velocity variations is well suited to estimate mass movements in an area, in that it allows to describe the tectonic activity of geologic structures and hydrothermal bodies. This enables to survey the background against induced flow and displacement patterns, which is crucial information for any reservoir utilisation.

CRediT authorship contribution statement

T. Toledo: Conceptualization, Data curation, Formal analysis, Investigation, Methodology, Software, Validation, Visualization, Writing – original draft, Writing – review & editing. **A. Obermann:** Conceptualization, Formal analysis, Investigation, Methodology, Software, Supervision, Writing – review & editing. **A. Verdel:** Conceptualization, Formal analysis, Investigation, Methodology, Supervision, Writing – review & editing. **J.E. Martins:** Conceptualization, Formal analysis, Investigation, Methodology, Supervision, Writing – review & editing. **P. Jousset:** Conceptualization, Formal analysis, Funding acquisition, Investigation, Methodology, Project administration, Resources, Supervision, Writing – review & editing. **A.K. Mortensen:** Data curation, Investigation, Resources, Writing – review & editing. **K. Erbas:** Data curation, Funding acquisition, Funding acquisition, Investigation, Project administration, Resources, Writing – review & editing. **C.M. Krawczyk:** Formal analysis, Investigation, Resources, Supervision, Writing – review & editing.

Declaration of Competing Interest

I certify on behalf of the coauthors that there is no conflict of interest of the manuscript submitted.

Acknowledgements

This work is part of the Microgravimotis project. The authors thank Landsvirkjun (The National Power Company of Iceland) for providing data and access to the geothermal area and ISOR (Iceland Geosurvey) for providing seismic data and for the close collaborations.

Waveform data and associated metadata are archived at the GEOFON seismological archive, FDSN code 3P (2017–2021) (Erbas et al., 2021), and are embargoed until December 2025.

Appendix A. Supplementary data

Supplementary data to this article can be found online at https://doi.org/10.1016/j.jvolgeores.2022.107590.

References

Abril, C., Tryggvason, A., Gudmundsson, O., Steffen, R., 2021. Local earthquake tomography in the Tjörnes Fracture Zone (North Iceland). J. Geophys. Res. Solid Earth 126 (6). https://doi.org/10.1029/2020JB020212.

Acevedo, J., Fernández-Viejo, G., Llana-Fúnez, S., López-Fernández, C., Olona, J., 2019. Ambient noise tomography of the southern sector of the Cantabrian Mountains, NW Spain. Geophys. J. Int. 219 (1), 479–495. https://doi.org/10.1093/gji/ggz308.

Ágústsson, K., Blanck, H., Mortensen, A.K., Guðmundsson, A., 2020. The seismic network of Landsvirkjun/Iceland GeoSurvey in Krafla, NE-Iceland, and Some Results, Proceedings World Geothermal Congress, paper 13059.

Almagro Vidal, C., Zaccarelli, L., Pintori, F., Serpelloni, E., 2021. Hydrological effects on seismic-noise monitoring in Karstic Mediaa. Geophys. Res. Lett. 48.

Andreé, J., Ayarza, P., Schimmel, M., Palomeras, I., Ruiz, M., Carbonell, R., 2020. What can seismic noise tell us about the Alpine reactivation of the Iberian Massif? An example in the Iberian Central System. Solid Earth 11, 2499–2513.

Ármannsson, H., Gíslason, G., Torfason, H., 1986. Surface exploration of the Theistareykir high-temperature geothermal area, with special reference to the application of geochemical methods. Appl. Geochem. 1, 47–64.

Ármannsson, H., Kristmannsdóttir, H., Torfason, H., Ólafsson, M., 2000. Natural changes in unexploited high-temperature geothermal areas in Iceland. In: Proceedings World Geothermal Congress 2000, Kyushu, Tohoku, 28 May-10 June, pp. 521–526.

Árnason, K., 2020. New conceptual model for the magma-hydrothermal-tectonic system of Krafla, NE Iceland. Geosciences 10 (1). https://doi.org/10.3390/geosciences10010034.

Barajas, A., Poli, P., D'Agostino, N., Margerin, L., Campillo, M., 2021. Separation of poroelastic and elastic processes of an aquifer from tectonic phenomena using geodetic, seismic, and meteorological data in the Pollino Region, Italy. Geochem. Geophys. Geosyst. 22 (11).

Barmin, M., Ritzwoller, M., Levshin, A., 2001. A fast and reliable method for surface wave tomography. Pure Appl. Geophys. 158, 1351–1375. https://doi.org/10.1007/PL00001225.

Bensen, G.D., Ritzwoller, M.H., Barmin, M.P., Levshin, A.L., Lin, F., Moschetti, M.P., Shapiro, N.M., Yang, Y., 2007. Processing seismic ambient noise data to obtain reliable broad-band surface wave dispersion measurements. Geophys. J. Int. 169 (3), 1239–1260. https://doi.org/10.1111/j.1365-246X.2007.03374.x.

Blanck, H., Ágústsson, K., Gunnarsson, K., 2017a. Seismic monitoring in Theistareykir, Krafla and Námafjall: November 2016 to March 2017, *Landsvirkjun Report, LV-2017-046*.

Blanck, H., Ágústsson, K., Gunnarsson, K., 2017b. Seismic monitoring in Krafla and Námafjall, and Theistareykir: April to August 2017, *Landsvirkjun Report, LV-2017-086*.

Blanck, H., Ágústsson, K., Gunnarsson, K., 2018. Seismic monitoring in Krafla and Námafjall, and Theistareykir: November 2017 to November 2018, *Landsvirkjun Report, LV-2018-103*.

Blanck, H., Águústsdoóttir, T., Ágústsson, K., Gunnarsson, K., 2020. Seismic monitoring in Krafla and Námafjall, and Theistareykir: November 2018 to November 2019, *Landsvirkjun Report, LV-2020-003*.

Calò, M., Dorbath, C., 2013. Different behaviours of the seismic velocity field at Soultz-sous-Forêts revealed by 4D seismic tomography: case study of GPK3 and GPK2 injection tests. Geophys. J. Int. 194 (2), 1119–1137. https://doi.org/10.1093/gji/ggt153.

Crowder, E., Rawlinson, N., Cornwell, D.G., Sammarco, C., Galetti, E., Curtis, A., 2020. Robust elastic non-linear waveform inversion: Application to real data. Geophys. J. Int. 224 (2), 1197–1210.

Cubuk-Sabuncu, Y., Jónsdóttir, K., Caudron, C., Lecocq, T., Parks, M.M., Geirsson, H., Mordret, A., 2021. Temporal seismic velocity changes during the 2020 rapid inflation at Mt. Þorbjörn-Svartsengi, Iceland, using seismic ambient noise. Geophys. Res. Lett. 48 (11).

Darling, W.G., Ármannsson, H., 1989. Stable isotope aspects of fluid flow in the Krafla, Námajall and Theistareykir geothermal systems of northeast Iceland. Chem. Geol. 76, 197–213.

De Matteis, R., Vanorio, T., Zollo, A., Ciuffi, S., Fiordelisi, A., Spinelli, E., 2008. Three-dimensional tomography and rock properties of the Larderello-Travale geothermal area, Italy. Phys. Earth Planet. Inter. 168 (1), 37–48.

D'Hour, V., M. Schimmel, A. F. Do Nascimento, J. M. Ferreira, and H. C. Lima Neto (2015), Detection of subtle hydromechanical medium changes caused by a small-magnitude earthquake swarm in NE Brazil, Pure Appl. Geophys., 173(4), 1097–1113, doi:https://doi.org/https://doi.org/10.1007/s00024-015-1156-0.

Drouin, V., 2020. InSAR Monitoring of Krafla, Bjarnarflag and þeistareykir Geothermal Areas, *Landsvirkjun Report, LV-2020-038*.

Drouin, V., Sigmundsson, F., 2019. Countrywide Observations of Plate Spreading and Glacial Isostatic Adjustment in Iceland Inferred by Sentinel-1 Radar Interferometry, 2015–2018. Geophys. Res. Lett. 46 (14) https://doi.org/10.1029/2019GL082629.

Einarsson, P., 2008. Plate boundaries, rifts and transforms in Iceland. Jökull 58, 35–58.

Einarsson, P., Sæmundsson, K., 1987. Earthquake epicenters 1982–1985 and volcanic systems of Iceland (map), *Í.* Hlutarsins Eðli: Festschrift for Thorbjörn Sigurgeirsson, Menningarsjóður, Reykjavík Iceland.

Erbas, K., et al., 2020. Continuous Microgravity Monitoring in a Volcanic Geothermal Field: Integrated Observational Approach in Þeistareykir, NE Iceland. Proc. World Geothermal Congress 2020.

Erbas, K., Toledo, T., Naranjo, D., Metz, M., Rietz, F., Florian, F., Jousset, P., 2021. Dataset of the 3p Seismic Network at the Theistareykir Geothermal Area, Iceland. Other/Seismic Network, GFZ Data Services. https://doi.org/10.14470/8C7562967492.

Forster, F., Güntner, A., Jousset, P., Reich, M., Männel, B., Hinderer, J., Erbas, K., 2021. Environmental and anthropogenic gravity contributions at the Theistareykir geothermal field, North Iceland. Geothermal Energy 9 (26).

Gautason, B., Ármannsson, H., Árnason, K., Saemundsson, K., Flóvenz, O.G., Thórhallsson, S., 2000. Thoughts on the next steps in the exploration of the Theistareykir geothermal area (in Icelandic), *Orkustofnun BG-HÁ-KÁ-KS-ÓGF-STh-2000/04*.

Gautason, B., et al., 2010. Exploration drilling in the Theistareykir high-temperature field, NE-Iceland: Stratigraphy, alteration and its relationship to temperature structure. In: Proceedings World Geothermal Congress 2010. Bali, Indonesia, 25–29 April.

Gíslason, G., Johnsen, G., Ármannsson, H., Torfason, H., Árnason, K., 1984. Theistareykir. Surface exploration of the high-temperature geothermal area (in Icelandic), *Orkustofnun, report OS-84089/JHD-16*.

Granados, I., Calò, M., Figueroa, A., Jousset, P., 2020. 3D Anisotropic velocity model of the Los Humeros geothermal field, Mexico, using seismic ambient noise tomography, *EGU General Assembly 2020,* Vienna, Austria. https://doi.org/10.5194/egusphere-egu2020-12544.

Grönvold, K., Karlsdóttir, R., 1975. Theistareykir. An interim report on the surface exploration of the geothermal area (In Icelandic), *NEA Report No. JHD 7501*, p. 37.

Hable, S., Sigloch, K., Stutzmann, E., Kiselev, S., Barruol, G., 2019. Tomography of crust and lithosphere in the western Indian Ocean from noise cross-correlations of land and ocean bottom seismometers. J. Geophys. Res. 219 (2), 924–944. https://doi.org/10.1093/gji/ggz333.

Hadziioannou, C., Larose, E., Coutant, O., Roux, P., Campillo, M., 2009. Stability of monitoring weak changes in multiply scattering media with ambient noise correlation: Laboratory experiments. J. Acoust. Soc. Am. 125 (6), 3688–3695. https://doi.org/10.1121/1.3125345.

Hadziioannou, C., Larose, E., Baig, A., Roux, P., Campillo, M., 2011. Improving temporal resolution in ambient noise monitoring of seismic wave speed. J. Geophys. Res. *116* (B07), 304. https://doi.org/10.1029/2011JB008200.

Herrmann, R.B., 2013. Computer programs in seismology: an evolving tool for instruction and research. Seismol. Res. Lett. 84, 1081–1088. https://doi.org/10.1785/0220110096.

Hillers, G., Husen, S., Obermann, A., Planès, T., Larose, E., Campillo, M., 2015. Noise-based monitoring and imaging of aseismic transient deformation induced by the 2006 Basel reservoir stimulation. Geophysics 80 (4). KS51–KS68.

Jousset, P., Haberland, C., Bauer, K., Arnasson, K., 2011. Hengill geothermal volcanic complex (Iceland) characterized by integrated geophysical observations. Geothermics 40 (1), 1–24. https://doi.org/10.1016/j.geothermics.2010.12.008.

Karastathis, V., Papoulia, J., Fiore, B.D., Makris, J., Tsambas, A., Stampolidis, A., Papadopoulos, G., 2011. Deep structure investigations of the geothermal field of the North European Gulf, Greece, using 3-D local earthquake tomography and Curie point depth analysis. J. Volcanol. Geotherm. Res. 206 (3), 106–120.

Karlsdóttir, R., Eysteinsson, H., Magnússon, I.T., Árnason, K., Kaldal, I., 2006. Tem measurements at Theistareykir and Gjástykki 2004–2006 (in Icelandic), *Iceland GeoSurvey, ÍSOR-2006/028*, p. 87.

Karlsdóttir, R., Vilhjálmsson, A.M., Árnason, K., Beyene, A.T., 2012. Theistareykir Geothermal Area, Northern Iceland: 3D inversion of MT and TEM data, *Report ÍSOR-2012/046*, pp. 1–173.

Khodayar, M., Björnsson, S., 2013. Preliminary fracture analysis of Theistareykir geothermal field and surroundings, Northern Rift Zone and Tjörnes Fracture Zone, *Landsvirkjun Report, LV-2013-116*.

Khodayar, M., Björnsson, S., Karlsdóttir, R., Ágústsson, K., Ólafsson, M., 2015. Tectonic control of alteration, gases, resistivity, magnetics and gravity in Theistareykir area. Implications for Northern Rift Zone and Tjörnes Fracture Zone, *Landsvirkjun Report, LV-2015-039*.

Khodayar, M., Björnsson, S., Kristinsson, S.G., Karlsdóttir, R., Ólafsson, M., Víkingsson, S., 2018. Tectonic control of the Theistareykir geothermal field by rift and transform zones in North Iceland: a multidisciplinary approach. Open J. Geol. 8, 543–584.

Kissling, E., 1988. Geotomography with local earthquake data. Rev. Geophys. 26, 659–698.

Kristinsson, S.G., Friðriksson, T., Ólafsson, M., Gunnarsdóttir, S.H., Níelsson, S., 2013a. Háhitasvæðin á Þeistareykjum, í Kröflu og Námafjalli. Vöktun á yfirborðsvirkni og grunnvatni., *Iceland GeoSurvey, ISOR-2013/037, LV-2013-091*.

Kristinsson, S.G., Óskarsson, F., Ólafsson, M., Óladóttir, A.A., Tryggvason, H., Friðriksson, T., 2013b. Háhitasæðin í Námafjalli, Kröflu og á Þeistareykjum. Vöktun á yfirborðsvirkni og grunnvatni árið 2013, *Iceland GeoSurvey, ISOR-2013/060, LV-2013-132*.

Kristinsson, S.G., Óskarsson, F., Óladóttir, A.A., Ólafsson, M., 2015. The High Temperature Geothermal Areas at Þeistareykir, Krafla and Námafjall. Monitoring of Surface Geothermal Activity and Groundwater in the Year 2015, *Iceland GeoSurvey, Report ÍSOR-2015/059, LV-2015-125*.

Landsvirkjun, 2016. Geothermal Power Station at Theistareykir: Energy Utilisation in Northeast Iceland. Landsvirkjun 2016 newsletter.

Layugan, D.B., 1981. Geoelectrical soundings and its application in the theistareykir high-temperature area. UNU-GTP, Iceland, report 5, 101.

Lecocq, T., Caudron, C., Brenguier, F., 2014. MSNoise, a Python package for monitoring seismic velocity changes using ambient seismic noise. Seismol. Res. Lett. 85, 715–726.

Lehujeur, M., Vergne, J., Maggi, A., Schmittbuhl, J., 2017. Ambient noise tomography with non-uniform noise sources and low aperture networks: case study of deep geothermal reservoirs in northern Alsace, France. Geophys. J. Int. 208 (1), 193–210.

Levshin, A., Yanocskaya, T., Lander, A., Bukchin, B., Barmin, M., Ratnikova, L., Its, E., 1989. Seismic Surface Waves in a Laterally Inhomogeneous Earth. Springer-Verlag.

Lobkis, O., Weaver, R., 2003. Coda-wave interferometry in finite solids: recovery of P-to-S conversion rates in an elastodynamic billiard. Phys. Rev. Lett. 90 (254), 302. https://doi.org/10.1103/PhysRevLett.90.254302.

Magnúsdóttir, S., Brandsdóttir, B., 2011. Tectonics of the Þeistareykir fissure swarm. Jökull 61.

Martins, J.E., Obermann, A., Verdel, A., Jousset, P., 2020a. 3-D S wave velocity model of the Los Humeros geothermal field, Mexico, by ambient-noise tomography, *Abstract from EGU General Assembly 2020,* Vienna, Austria. https://doi.org/10.5194/egusphere-egu2020-21956.

Martins, J.E., Weemstra, C., Ruigrok, E., Verdel, A., Jousset, P., Hersir, G.P., 2020b. 3D S-wave velocity imaging of Reykjanes Peninsula high-enthalpy geothermal fields with ambient-noise tomography. J. Volcanol. Geotherm. Res. 391 (106), 685. https://doi.org/10.1016/j.jvolgeores.2019.106685.

Meier, U., Shapiro, N.M., Brenguier, F., 2010. Detecting seasonal variations in seismic velocities within los Angeles basin from correlations of ambient seismic noise. Geophys. J. Int. 181 (2).

Metzger, S., Jónsson, S., Geirsson, H., 2011. Locking depth and slip-rate of the Húsavík Flatey fault, North Iceland, derived from continuous GPS data 2006-2010. Geophys. J. Int. 187 (2), 564–576. https://doi.org/10.1111/j.1365-246X.2011.05176.x.

Mordret, A., Landès, M., Shapiro, N.M., Singh, S., Roux, P., Barkved, O., 2013. Near-surface study at the Valhall oil field from ambient noise surface wave tomography. Geophys. J. Int. 193 (3), 1627–1643.

Mordret, A., Landès, M., Shapiro, N.M., Singh, S., Roux, P., 2014. Ambient noise surface wave tomography to determine the shallow shear velocity structure at Valhall: depth inversion with a Neighbourhood Algorithm. Geophys. J. Int. 198 (3), 1514–1525. https://doi.org/10.1093/gji/ggu217.

Mordret, A., Rivet, D., Landès, M., Shapiro, N.M., 2015. Three-dimensional shear velocity anisotropic model of Piton de la Fournaise Volcano (La Réunion Island) from ambient seismic noise. J. Geophys. Res. Solid Earth 120, 406–427. https://doi.org/10.1002/2014JB011654.

Muksin, U., Bauer, K., Haberland, C., 2013. Seismic Vp and Vp/Vs structure of the geothermal area around Tarutung (North Sumatra, Indonesia) derived from local earthquake tomography. J. Volcanol. Geotherm. Res. 260, 27–42. https://doi.org/10.1016/j.jvolgeores.2013.04.012.

Nakata, N., Gualtieri, L., Fichtner, A. (Eds.), 2019. Seismic Ambient Noise. Cambridge University Press. https://doi.org/10.1017/9781108264808.

Naranjo, D., 2020. Seismological Characterization of the Theistareykir Geothermal Field (Iceland). Master Thesis. IDEA League-ETH Zurich.

Obermann, A., Hillers, G., 2019. Chapter two - seismic time-lapse interferometry across scales. Adv. Geophys. 60, 65–143. https://doi.org/10.1016/bs.agph.2019.06.001.

Obermann, A., Kraft, T., Larose, E., Wiemer, S., 2015. Potential of ambient seismic noise techniques to monitor the St. Gallen geothermal site (Switzerland). J. Geophys. Res. Solid Earth 120 (6), 4301–4316. https://doi.org/10.1002/2014JB011817.

Obermann, A., Lupi, M., Modret, A., Jakobsdóttir, S.S., Miller, S.A., 2016. 3D-ambient noise Rayleigh wave tomography of Snæfellsjökull volcano, Iceland. J. Volcanol. Geotherm. Res. 317, 42–52.

Óskarsson, F., 2011. Háhitaholur á Þeistareykjum. efnasamsetning vökva og gufu, *Iceland GeoSurvey, report, ISOR-2011/068*.

Pedersen, R., Sigmundsson, F., Masterlark, T., 2009. Rheologic controls on inter-rifting deformation of the Northern Volcanic Zone, Iceland. Earth Planet. Sci. Lett. 281 (1–2), 14–26. https://doi.org/10.1016/j.epsl.2009.02.003.

Planès, T., Obermann, A., Antunes, V., Lupi, M., 2020. Ambient-noise tomography of the Greater Geneva Basin in a geothermal exploration context. Geophys. J. Int. 220, 370–383. https://doi.org/10.1093/gji/ggz457.

Portier, N., et al., 2020. 2017-2019 hybrid micro-gravity monitoring of the Theistareykir geothermal field (North Iceland). EGW 2020.

Ratdomopurbo, A., Poupinet, G., 1995. Monitoring a temporal change of seismic velocity in a volcano: Application to the 1992eruption of Mt. Merapi (Indonesia). Geophys. Res. Lett. 22 (7), 775–778.

Rivet, D., Brenguier, F., Cappa, F., 2015. Improved detection of preeruptive seismic velocity drops at the piton de la fournaise volcano. Geophys. Res. Lett. 42, 6332–6339.

Saemundsson, K., 1979. Outline of the geology of Iceland. Jökull 29, 7–28.

Saemundsson, K., 2007. The Geology of Theistareykir (in Icelandic), *Iceland GeoSurvey, Report ÍSOR-07270*.

Saemundsson, K., Hjartarson, A., Kaldal, I., Sigurgeirsson, S.G.M.Á., Kristinsson, Víkingsson, S., 2012. Geological Map of Northern Volcanic Zone, Iceland. Northern Part. 1:100.000. Reykjavík, Iceland, Iceland GeoSurvey and Landsvirkjun.

Sambridge, M., 1999. Geophysical inversion with a neighborhood algorithm. I. Searching a parameter space. Geophys. J. Int. 138 (2), 479–494.

Sánchez-Pastor, P., Obermann, A., Schimmel, M., 2018. Detecting and locating precursory signals during the 2011 El Hierro, Canary Islands. Geophys. Res. Lett. 45 (19), 10,288–10,297. https://doi.org/10.1029/2018GL079550.

Sánchez-Pastor, P., Obermann, A., Schimmel, M., Weemstra, C., Verdel, A., Jousset, P., 2019. Short- and long-term variations in the Reykjanes geothermal reservoir from seismic noise interferometry. Geophys. Res. Lett. 46 (11), 5788–5798. https://doi.org/10.1029/2019GL082352.

Sánchez-Pastor, P., Obermann, A., Reinsch, T., Ágústsdóttir, T., Hjörleifsdóttir, V., Wiemer, S., 2021. Imaging high-temperature geothermal reservoirs with ambient seismic noise tomography, a case study of the Hengill geothermal field, SW Iceland. Geothermics. https://doi.org/10.1016/j.geothermics.2021.102207.

Schimmel, M., 1999. Phase cross-correlations: Design, comparisons, and applications. Bull. Seismol. Soc. Am. 89.

Schimmel, M., Stutzmann, E., Gallart, J., 2011. Using instantaneous phase coherence for signal extraction from ambient noise data at a local to a global scale. Geophys. J. Int. 184 (1), 494–506. https://doi.org/10.1111/j.1365-246X.2010.04861.x.

Schimmel, M., Stutzmann, E., Ventosa, S., 2018. Low-frequency ambient noise autocorrelations: Waveforms and normal modes. Geophys. J. Int. 89 (4), 1488–1496. https://doi.org/10.1785/0220180027.

Sens-Schönfelder, C., Wegler, U., 2006. Passive image interferometry and seasonal variations of seismic velocities at Merapi Volcano, Indonesia. Geophys. Res. Lett. 33 (21) https://doi.org/10.1029/2006GL027797.

Shapiro, N.M., Campillo, M., Stehly, L., Ritzwoller, M.H., 2005. High resolution surface-wave tomography from ambient seismic noise. Science 307 (5715), 1615–1618.

Snieder, R., 2002. Coda wave interferometry and the equilibration of energy in elastic media. Phys. Rev. E Stat. Nonlinear Soft Matter Phys. 66 (046), 615.

Spaans, K., Sigmundsson, F., Hreinsdóttir, S., 2012. Crustal Deformation in the Kraa, Gjástykki and Theistareykir Areas Inferred from GPS and InSAR Techniques, *Status Report.* Institute of Earth Sciences. University of Iceland, p. 23.

Stefánsson, R., et al., 1993. Earthquake prediction research in the South Iceland seismic zone and the SIL project. Bull. Seismol. Soc. Am. 83 (3), 696–716.

Stefánsson, R., Guðmundsson, G.B., Halldórsson, P., 2008. Tjörnes Fracture Zone. New and old seismic evidences for the link between the North Iceland Rift Zone and the Mid-Atlantic Ridge. Tectonophysics 447, 117–126. https://doi.org/10.1016/j.tecto.2006.09.019.

Stutzmann, E., Schimmel, M., Patau, G., Maggi, A., 2009. Global climate imprint on seismic noise. Geochem. Geophys. Geosyst. *10* (Q11), 004. https://doi.org/10.1029/2009GC002619.

Taira, T., Nayak, A., Brenguier, F., Manga, M., 2018. Monitoring reservoir response to earthquakes and fluid extraction, Salton Sea geothermal field, California. Sci. Adv. 4 (1) https://doi.org/10.1126/sciadv.1701536.

Thoroddsen, T., 1983. Die Geschichte der Isländischen Vulkane. Det Kongelige Danske Vidernskabernes Selskab, Höst og Sön, Copenhagen.

Thorsteinsdóttir, U., Ásgeirsdóttir, R.S., Einarsson, G.M., Sigurgeirsson, M.A., Helgadóttir, H.M., Níelsson, S., 2018. Þeistareykir - Revision of the Geological and Alteration Model, *Landsvirkjun Report, LV-2018-054*.

Thurber, C.H., 1983. Earthquake locations and three-dimensional crustal structure in the Coyote Lake area, Central California. J. Geophys. Res. Solid Earth 88, 8226–8236.

Tibaldi, A., Bonali, F.L., Mariotto, F.P., Russo, E., Ranieri Tenti, L.M., 2019. The development of divergent margins: Insights from the North Volcanic Zone, Iceland. Earth Planet. Sci. Lett. 509, 1–8.

Tibaldi, A., Bonali, F.L., Mariotto, F.P., Corti, N., Russo, E., Einarsson, P., Hjartardóttir, A.R., 2020. Rifting kinematics produced by magmatic and tectonic stresses in the North Volcanic Zone of Iceland, *Frontiers*. Earth Sci. 8 (174) https://doi.org/10.3389/feart.2020.00174.

Toledo, T., Jousset, P., Maurer, H., Krawczyk, C., 2018. Optimized experimental network design for earthquake location problems: applications to geothermal and volcanic field seismic networks. J. Volcanol. Geotherm. Res. https://doi.org/10.1016/j.jvolgeores.2018.08.011, 0377–0273.

Toledo, T., Gaucher, E., Jousset, P., Jentsch, A., Haberland, C., Maurer, H., Krawczyk, C., Calò, M., Figueroa, A., 2020. Local earthquake tomography at Los Humeros geothermal field (Mexico). J. Geophys. Res. Solid Earth 125. https://doi.org/10.1029/2020JB020390.

Vanorio, T., Virieux, J., Capuano, P., Russo, G., 2005. Three-dimensional seismic tomography from P wave and S wave microearthquake travel times and rock physics characterization of the Campi Flegrei Caldera. J. Geophys. Res. Solid Earth *110* (B03), 201. https://doi.org/10.1029/2004JB003102.

Ventosa, S., Schimmel, M., Stutzmann, E., 2019. Towards the processing of large data volumes with phase cross-correlation. Seismol. Res. Lett. 90 (4), 1663–1669. https://doi.org/10.1785/0220190022.

Wapenaar, K., 2004. Retrieving the elastodynamic Green's function of an arbitrary inhomogeneous medium by cross correlation. Phys. Rev. Lett. 93 (25), 254,301.

Wapenaar, K., Fokkema, J., 2006. Green's function representations for seismic interferometry. Geophysics 71 (4). SI33–SI46.

Weaver, R.L., Hadziioannou, C., Larose, E., Campillo, M., 2011. On the precision of noise correlation interferometry. Geophys. J. Int. 185 (3), 1384–1392. https://doi.org/10.1111/j.1365-246X.2011.05015.x.